JACS
JOURNAL OF THE AMERICAN CHEMICAL SOCIETY

ARTICLE

pubs.acs.org/JACS

A Cast-Mold Approach to Iron Oxide and Pt/Iron Oxide Nanocontainers and Nanoparticles with a Reactive Concave Surface

Chandramohan George,[†] Dirk Dorfs,[†] Giovanni Bertoni,[†] Andrea Falqui,[†] Alessandro Genovese,[†] Teresa Pellegrino,[†,‡] Anna Roig,[§] Alessandra Quarta,[‡] Roberto Comparelli,[∥] M. Lucia Curri,[∥] Roberto Cingolani,[†] and Liberato Manna*[,†]

[†]Istituto Italiano di Tecnologia, Via Morego 30, 16163 Genova, Italy

[‡]Nanoscience Institute of CNR, via Arnesano 16, 73100 Lecce, Italy

[§]Institut de Ciència de Materials de Barcelona (ICMAB-CSIC), Campus de la UAB, 08913 Bellaterra, Spain

[∥]CNR, Istituto per i Processi Chimico-Fisici, via Orabona 4, 73100 Bari, Italy

Supporting Information

ABSTRACT: We report the synthesis of various iron oxide nanocontainers and Pt−iron oxide nanoparticles based on a cast-mold approach, starting from nanoparticles having a metal core (either Au or AuPt) and an iron oxide shell. Upon annealing, the particles evolve to asymmetric core−shells and then to heterodimers. If iodine is used to leach Au out of these structures, asymmetric core−shells evolve into "nanocontainers", that is, iron oxide nanoparticles enclosing a cavity accessible through nanometer-sized pores, while heterodimers evolve into particles with a concave region. When starting from a metal domain made of AuPt, selective leaching of the Au atoms yields the same iron oxide nanoparticle morphologies but now encasing Pt domains (in their concave region or in their cavity). We found that the concave nanoparticles are capable of destabilizing Au nanocrystals of sizes matching that of the concave region. In addition, for the nanocontainers, we propose two different applications: (i) we demonstrate loading of the cavity region of the nanocontainers with the antitumoral drug *cis*-platin; and (ii) we show that nanocontainers encasing Pt domains can act as recoverable photocatalysts for the reduction of a model dye.

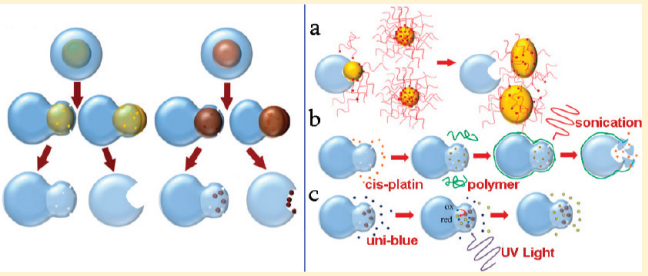

1. INTRODUCTION

For many years, iron oxide-based nanostructures have been synthesized and exploited in drug delivery, magnetic resonance imaging, ferrofluids, catalysis, gas sensing, and lithium ion batteries.[1−8] Nowadays, the synthesis of new nanostructures out of this material, in terms of desired morphology, chemical composition, and stability, is a clearly demanding task. On the other hand, hollow colloidal inorganic nanoparticles (NPs) with various morphologies (cage, box, frame, ring, tube, and wire-like) have recently emerged as an interesting class of materials, and also porous and interior hollow nanostructures (especially those based on magnetic oxides) have been synthesized.[9−11] Various approaches have been proposed for the synthesis of hollow inorganic NPs, most notably via chemical etching, galvanic replacement, via the Kirkendall effect and by using sacrificial templates.[12] Hollow NPs are thermodynamically less stable than their "filled" counterparts, due to their much higher surface to volume ratio, and their inner surface can provide effective sites for chemical reactions that can take place in a region that is "protected" from the external environment, and such hollow nanostructures could act as efficient nanocatalysts, as carriers for drug delivery and as nanocontainers for bioseparation and for removal of contaminants.[13]

Recently, Alivisatos et al. have reported the synthesis of hollow iron oxide nanospheres starting from iron NPs, by exploiting the Kirkendall effect,[14] and Sun et al. have shown how leaching of gold from colloidal Au−iron oxide heterodimers yields iron oxide NPs with a concave region.[15] Here, we further elaborate the "cast-mold" procedure of Sun by first synthesizing core−shell NPs of Au−iron oxide and AuPt−iron oxide, and we show that, upon annealing, all these NPs were reshaped to asymmetric core−shells and then to heterodimers. We then used iodine to leach Au atoms out of the NPs. Upon this treatment, Au−iron oxide asymmetric core−shells evolved into iron oxide NPs carrying a cavity that was accessible from the external environment through nanometer-sized pores, while Au−iron oxide asymmetric heterodimers evolved into NPs with a concave region (see Scheme 1a). Hence, the degree of annealing of the initial heterostructures was critical in defining their overall morphology, which in turn yielded either concave NPs or nanocontainers upon Au leaching. When instead the metal domain was made of an AuPt alloy, selective leaching of the Au atoms led to the same morphologies for the iron oxide NPs as when starting

Received: September 29, 2010
Published: January 26, 2011

Scheme 1. Sketch Highlighting the Various Morphologies of Colloidal (a) Iron Oxide and (b) Iron Oxide−Pt NPs Obtained by Annealing Au−Iron Oxide and AuPt−Iron Oxide Heterostructures, Followed by Leaching of the Gold Atoms[a]

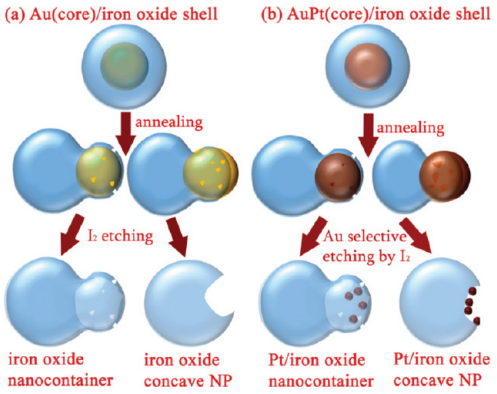

[a] Bottom models, from left to right: iron oxide nanocontainers, concave NPs, and the respective nanostructures encasing Pt domains.

from Au−iron oxide NPs, that is, nanocontainers or concave NPs. This time, however, because Pt atoms could not be leached out, the NPs in addition carried Pt domains (1−3 nm in size) encased in their structures (see Scheme 1b).

One fascinating property of the concave NPs appears to be their capability to destabilize Au nanocrystals of appropriate sizes (see Scheme 2a). When concave NPs were mixed with colloidal spherical Au nanocrystals, whose diameter was comparable to that of their concave region, the Au nanocrystals started aggregating and forming much larger nanocrystals, while the concave NPs remained stable in solution. Such aggregation/ripening process was not observed when instead the concave NPs were mixed with Au nanocrystals that were much larger or much smaller than the concave region. Therefore, our observations indicate that only when the Au nanocrystals could occupy almost entirely the volume of the concave region of such NPs, thus forming a key-lock assembly, then could the Au nanocrystal surface interact strongly with the concave surface of the iron oxide NPs. This interaction tended to destabilize the Au nanocrystals, most likely via mechanical friction that caused partial stripping of surfactant molecules bound to the Au surface atoms.

Furthermore, we propose here two applications for the iron oxide nanocontainers. As a first application, we have explored the feasibility to load *cis*-platin (an anticancer drug for the treatment of various types of tumors)[16,17] inside the cavity region of the nanocontainers (Scheme 2b). This follows a recent study by Sun et al. who tested porous hollow iron oxide NPs (also prepared by colloidal approaches) as storage units for the *cis*-platin,[9] as well as other works that have exploited various systems (liposomes, polymeric capsules, and inorganic NPs) as containers or as anchoring structures for the drug.[9,18−24] As compared to *cis*-platin cargo systems based on liposomes or polymeric particles, the use of a magnetic nanostructure might offer the unique advantage of being magnetically manipulated and driven to the tumor site, thus improving the targeting efficiency,[25] while keeping the overall nanocontainer size much smaller than that of the carriers currently used for *cis*-platin. We found that our iron oxide nanocontainers, once coated by a suitable polymer shell that makes them water-soluble, had a loading capability for *cis*-platin 6 times higher than that of their parent core/shell Au−iron oxide NPs (likewise coated by a polymer shell). One interesting aspect of the present nanocontainers, which is not limited to drug loading, is that the nanocontainer region (thin membrane) could be broken by sonication under mild conditions, thus providing a potential mechanism for cargo release.

As another application, we tested the photocatalytic behavior of nanocontainers encasing Pt domains (Scheme 2c). In photocatalysis, improved charge separation and inhibition of charge carrier recombination are essential in enhancing the overall efficiency for interfacial charge transfer,[26−28] and there are recent reports showing how this was achieved efficiently in colloidal nanocrystals made of metal and semiconductor domains attached together.[29−33] In the case of our nanocontainers, one potential advantage over previously reported metal−semiconductor catalysts is that the Pt domains lie inside the cavity region of the NPs, and hence they are protected from the external environment, while they are still accessible to chemical species. Besides, because the nanocontainers combine photocatalytic and magnetic properties, they are appealing for microheterogeneous catalytic applications. We studied the photoreduction of the model organic dye Uniblue-A (UBA) in the presence of nanocontainers (both iron oxide only and iron oxide−Pt ones). This dye undergoes a color change when converting from the oxidized anthraquinonic structure (blue) to the reduced hydroanthraquinonic structure (yellow), due to different electron conjugations in these two structures.[34] We found that the dye bleached faster in the presence of Pt/iron oxide nanocontainers than in the presence of iron oxide-"only" nanocontainers. In all cases, the nanocontainers remained stable and unchanged in morphology/composition and could be recovered by magnetic separation.

2. EXPERIMENTS

2.1. Chemicals. All chemicals were of the highest purity available and were used as received without further purification. The following chemicals were purchased from Sigma-Aldrich: iron(0) carbonyl [$Fe(CO)_5$] (99.99%), gold(III) chloride, $AuCl_3$ (99%), didecyldimethylammoniumbromide (DDAB) $[CH_3(CH_2)_9]_2N(CH_3)_2Br$ (98%), iodine (I_2, 99.999% trace metals basis), platinum(II) acetylacetonate ($Pt(C_5H_7O_2)_2$, 99.99% trace metals basis), 1,2-hexadecanediol ($CH_3(CH_2)_{13}CHOHCH_2OH$, technical grade 90%), *cis*-diammineplatinum(II) dichloride ($Pt(NH_3)_2Cl_2$, ≥99.9% trace metals basis, henceforth referred to as "*cis*-platin"), tetramethylammonium hydroxide solution ($(CH_3)_4N(OH)$, 25 wt % in H_2O), oleylamine (70%), oleic acid (90%), 1-octadecene (ODE, 90%), and Uniblue A (UBA, sodium salt, MW 506.49). Sodium borohydride (~98%) was purchased from Sigma. *N*,*N*-Dimethylformamide (analytical grade), anhydrous ethanol, toluene, hexane, and chloroform were purchased from Carlo Erba reagents. Ultrapure water (18 MΩ) was used for preparing buffer solutions.

2.2. Synthesis Procedure. Oleylamine-coated Au nanocrystals were prepared by reducing $AuCl_3$ by $NaBH_4$ in a micellar solution of DDAB followed by the functionalization of Au nanocrystals with oleylamine. To prepare AuPt alloy NPs, $Pt(C_5H_7O_2)_2$ was reacted with the Au nanocrystals in the presence of 1,4 hexadecanediol, which induced the reduction of Pt on the gold surface. Upon annealing the NPs at 300 °C for 2.5 h, Pt diffused into the Au cores (Supporting Information Figure S1). In analogy with Sun's approach,[35] the metal NPs (either Au or AuPt) were reacted with $Fe(CO)_5$ in octadecene to grow metal−iron oxide core−shell NPs. By varying the reaction temperature from 190 to 320 °C and the reaction time from 30 min to 4 h, the initial core−shell NPs evolved into various asymmetric metal−metal oxide core−shell morphologies[36] and then to heterodimers, in which it was possible to tune the degree of exposure of the metal

Scheme 2. Sketches of (a) Destabilization of Nanocrystals Using Concave Iron Oxide NPs; (b) Loading of Iron Oxide Nanocontainers with *cis*-Platin Molecules, Coating with a Polymer Shell That Makes Them Water-Soluble, and Sonication That Breaks the Container Region; and (c) Heterogeneous Photocatalytic Reduction of Uniblue-A by Easily Recoverable and Reusable Pt/Iron Oxide Nanocontainers

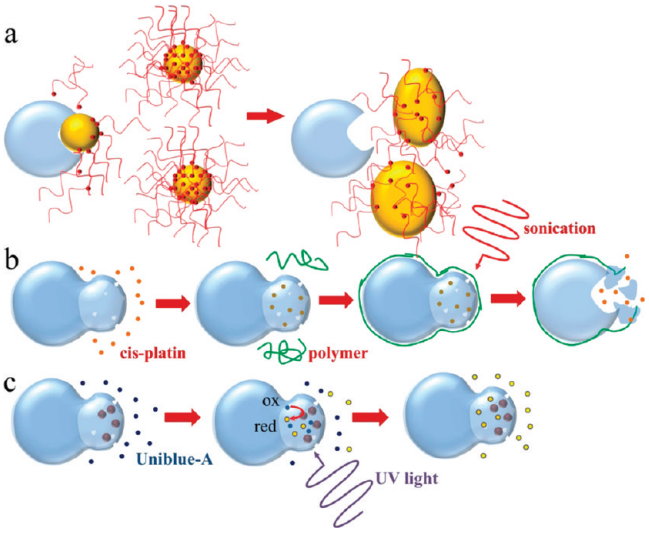

domain to the external environment (see Scheme 1 and Supporting Information Figure S2). In both cases, the gold atoms could be selectively dissolved via treatment with iodine molecules, and either iron oxide NPs enclosing an accessible cavity, that is, "nanocontainers", or concave NPs were formed (Figure 1). In the concave NPs, the size of the cavity could be tuned by changing the size original gold region (Supporting Information Figures S2 and S3). The resulting NPs were washed several times with a mixture of 1:1 ethanol/toluene through centrifugation and were finally redispersed in hexane or toluene.

2.3. Morphological, Structural, and Compositional Analysis by Transmission Electron Microscopy (TEM), Scanning TEM (STEM), High-Resolution TEM (HRTEM), Energy Filtered TEM (EFTEM), and Energy Dispersive Spectroscopy (EDS-STEM) Measurements. TEM images were recorded on a JEOL JEM 1011 microscope, equipped with a W electron source and operating at 100 kV. Scanning TEM (STEM) in high angle annular dark field (HAADF) mode, high-resolution TEM (HRTEM), and energy filtered (EFTEM) measurements were performed on a JEOL JEM-2200FS microscope, equipped with a field emission gun (FEG) working at an accelerating voltage of 200 kV, an objective lens (OL) CEOS spherical aberration corrector, an Omega energy filter, and a EDS spectrometer with Si(Li) detector. Energy filtered images were acquired using a contrast aperture of about 10 mrad to reduce aberrations (mostly chromatic). Chemical maps from Fe L (708 eV) and O K (532 eV) edges were obtained by acquiring three images (one post-edge and two pre-edge), respectively, to extract the background, with an energy slit of 30 eV for Fe and 20 eV for O. The samples for TEM analysis were prepared in a glovebox by depositing a few drops of a dilute solution of nanocrystals onto carbon-coated Cu grids. The latter were then transferred immediately into the microscope. Cryo-STEM experiments were carried out by depositing a drop of solution on a holey carbon coated TEM grid, followed by fast blotting to form a thin film of frozen solution. The grid was then immediately dipped into liquid nitrogen, transferred in a cryo-holder, and observed in STEM while still at cryogenic temperature (about 90 K).

2.4. X-ray Powder Diffraction (XRD). XRD measurements were performed with a Rigaku SmartLab X-ray diffractometer. Concentrated nanocrystal solutions were spread on top of silicon substrate, after which the sample was allowed to dry and was then measured in parallel beam reflection geometry $2\theta/\omega$ using Cu Kα wavelength. For phase identification, we used PDXL software of Rigaku.

2.5. Optical Characterization. Optical absorption measurements on nanocrystal solutions were carried out using a Varian Cary 5000 UV−vis−NIR spectrophotometer. Nanocrystals were dispersed in toluene. For the photocatalytic studies (see section 2.9), UV−Vis absorption spectra were recorded with a UV−vis−NIR Cary 5 (Varian) spectrophotometer. In those experiments, the nanocrystals were dissolved instead in a $CHCl_3$:EtOH solution.

2.6. Magnetic Characterization. Magnetization versus applied magnetic field at 298 K and zero-field cooled (ZFC)−field cooled (FC) curves with a 50 Oe applied field were measured using a superconducting quantum interference device (SQUID) magnetometer (Quantum Design MPMS5XL). The samples were prepared using a plastic capsule filled with packed cotton, which was impregnated with a known hexane solution of nanocrystals and was then dried. Experimental results were corrected for the sample holder contribution.

2.7. Destabilization Experiments Using Concave NPs. In all of the experiments, as a first step fresh oleylamine (1−2 μL) was added to the solution of concave NPs to passivate their concave region, because after Au leaching this region had been left uncoated by surfactants. However, it is likely that this addition of oleylamine cannot passivate effectively the entire concave region and its proximity because the concave particles show a strong tendency to aggregate (see section 3.2). A solution of concave NPs was then mixed with a solution of colloidal spherical Au nanocrystals[37] at a known concentration (about 10^{-8} M for both Au nanocrystals and concave iron oxide NPs) of all components (see Supporting Information Figure S6). The resulting mixture was monitored over time via dynamic light scattering (using a Malvern Instruments Zeta Sizer equipped with a 4.0 mW He−Ne laser operating at 633 nm and an avalanche photodiode detector) and optical absorption spectroscopy (for these measurements, the original mixture was diluted 1:25), and aliquots of the solution were examined under TEM. Various experiments were carried out to identify the appropriate size of the concave region to be efficient for "destabilizing" the NPs. In three series of experiments, the concave NPs were mixed with Au nanocrystals having diameters that were respectively smaller (5 nm), matching size (12 nm) and larger (20 nm), and matching the diameter of the concave region. Also, several control experiments were run. These are described in detail in the Supporting Information.

2.8. *cis*-Platin Loading Experiments. First, 50 μL of a 25 mM *cis*-platin solution (prepared by dissolving the drug in a mixture of chloroform and DMF 2:1, v/v) was added to 750 μL of a solution of NPs (either the parent Au−iron oxide heterodimers or the nanocontainers derived from them by Au leaching) dissolved in chloroform. In both series of experiments, the overall concentration of iron atoms in the resulting solution was 3 mM (concentrations were determined via elemental analysis). The solution was stirred overnight at room temperature, the solvent was then evaporated, and 2 mL of a solution of poly(maleic anhydride-*alt*-1-tetradecene) in chloroform (6.5×10^{-2} M) was added to the solid. Approximately 500 molecules of polymer monomer units were added per nm^2 of NP surface. The solution was stirred for 30 min, and thereafter the solvent was slowly removed by using a rotary evaporation system. Two milliliters of borate buffer (pH 9) was then added, and the solution was purified from excess *cis*-platin and polymer by applying an external magnet (0.3 T) close to the vial walls for approximately 4−5 h. After this time, the nanocrystals had accumulated quantitatively to the vial walls close to the magnet. The solution was replaced with fresh buffer, into which the NPs could be redissolved by removing the magnet. This cleaning procedure was applied at least three

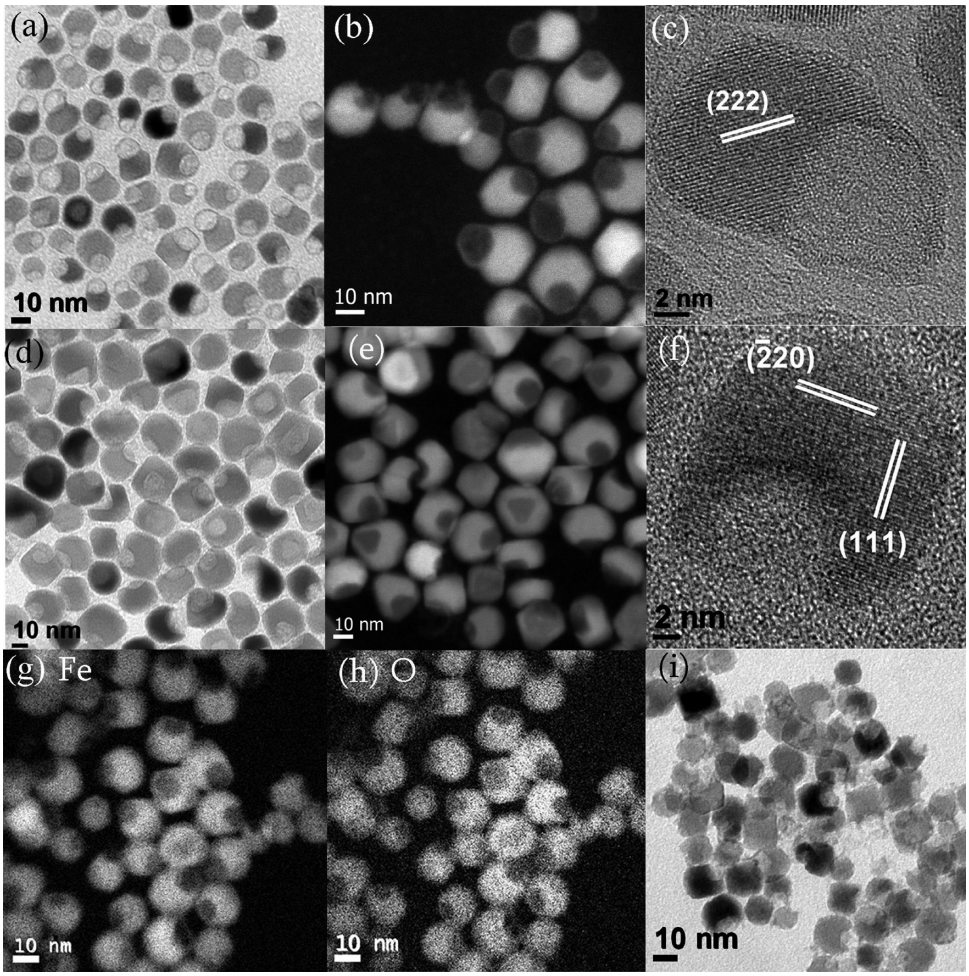

Figure 1. (a) Transmission electron microscopy (TEM) image of iron oxide nanocontainers; (b) high angle annular dark field (HAADF) STEM images of iron oxide nanocontainers; (c) HRTEM image of a single nanocontainer; (d) TEM, (e) HAADF-STEM, and (f) HRTEM images of concave iron oxide NPs; (g,h) energy filtered TEM (EFTEM) images of nanocontainers at the Fe L edge and O K edge, mapping the distribution of Fe and O; and (i) nanocontainers after 20 min of sonication at 100 W: the thin iron oxide membrane in each nanocontainer has been disrupted almost completely.

times to remove the polymer micelles and the excess *cis*-platin. Finally, the solution was filtered using a 0.5 μM filter to remove NP aggregates.

The *cis*-platin loading capacity was assessed by means of elemental analysis on the cleaned solution. The amount of Pt loaded was reported as the number of *cis*-platin molecules per NP (each *cis*-platin molecule contains 1 Pt atom). For both samples, the concentration of NPs was determined by combining results from elemental analysis (total concentration of Fe), TEM analysis (average size and morphology of the NPs), and by building a structural model of the NPs, using software developed by us.[38] Three independent series of loading experiments were carried out on both samples, and the results in terms of *cis*-platin loading per NP are reported here as averages over the three series.

2.9. Photocatalytic Studies. These were carried out to compare the photocatalytic behavior of iron oxide nanocontainers encasing Pt domains in the cavity region to that of iron oxide nanocontainers without Pt domains. A solution of NPs dissolved in hexane was dried under N_2 and was then redissolved in a mixture of chloroform and ethanol ($CHCl_3$:EtOH). The overall concentration of iron atoms in the resulting solution was 3 mM in all experiments (as determined via elemental analysis). Because of the low solubility of UBA in hexane, all experiments were performed in $CHCl_3$. For the studies carried out in the presence of UBA, the proper amount of a stock solution of UBA in EtOH (2.5×10^{-3} M) was added to reach the desired $CHCl_3$:EtOH ratio and fix the final UBA concentration at 10^{-5} M. A quartz cuvette was filled with the reaction mixture and sealed by a Teflon-faced rubber cap. All samples were preliminarily deaerated by N_2 purging for 20 min. Next, the mixture, kept under stirring, was UV-irradiated using a medium pressure 200 W mercury lamp ($\lambda > 250$ nm).

Test experiments were previously carried out to preliminary check the oxygen-free condition in the reaction cuvette: a suspension of commercially available TiO_2 (Degussa P25) in $CHCl_3$/EtOH was sealed airtight in a cuvette. Under UV irradiation in deaerated conditions, this suspension turned from white to blue in a few minutes, due to accumulation of electrons in the conduction band of TiO_2.[29] The blue color remained as long as an inert atmosphere was maintained in the quartz cuvette and promptly disappeared in the presence of air, as in this case oxygen molecules could quickly scavenge the accumulated electrons. The photocatalytic reactions were carried out in microheterogeneous catalyst $CHCl_3$/EtOH solutions. As the absorption signals of both UBA and of the catalysts NPs fell in the same spectral region (400−700 nm), the reaction was monitored by recording difference absorption spectra of the irradiated reaction mixtures. Any change in the absorption line-shape was then clearly identified for each sample, by considering as reference the respective unphotolyzed solution.

2.10. Elemental Analysis. Elemental analysis was carried out via inductively coupled plasma atomic emission spectroscopy (ICP-AES),

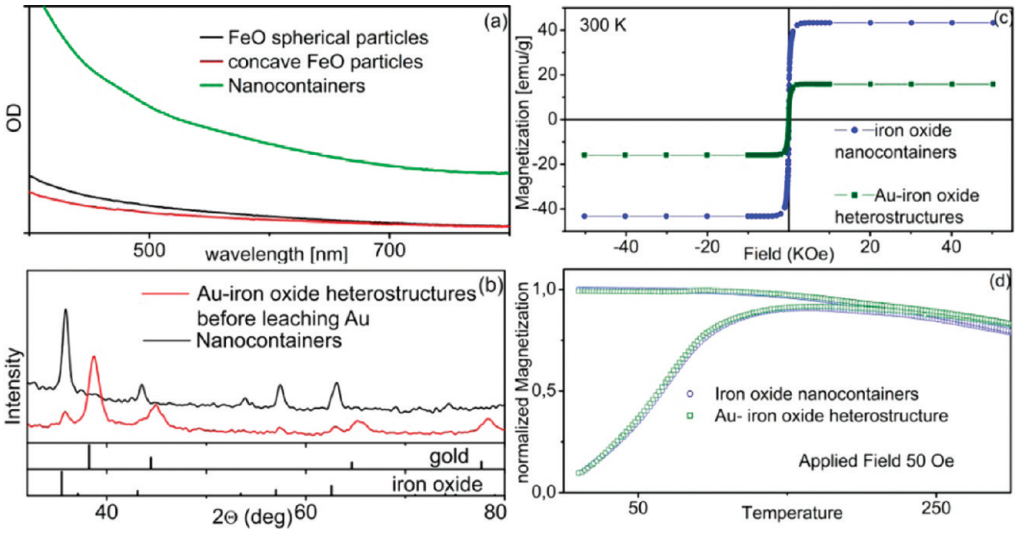

Figure 2. (a) UV−vis spectra of iron oxide nanocontainers and concave NPs. For comparison, a spectrum of spherical iron oxide NPs is shown. (b) XRD patterns of Au−iron oxide heterostructures and of the corresponding nanocontainers obtained after gold leaching. The XRD is compatible with both magnetite and maghemite structures. (c) Magnetization behavior of Au−iron oxide heterostructures and of the corresponding nanocontainers. (d) ZFC-FC curves of the same samples.

using a Varian Vista AX spectrometer. Samples were dissolved in HCl/HNO_3 3:1 (v/v).

3. RESULTS AND DISCUSSION

3.1. Structural, Optical, and Magnetic Investigation of the Nanostructures. Two main parameters controlled the different morphologies of the nanostructures: (i) the size of the initial Au or PtAu nanocrystals on which the iron oxide shell was initially grown, which dictated the size of the concave region or of the container region of the iron oxide nanostructures upon annealing and Au leaching; and (ii) the annealing conditions (temperature and time of annealing), which dictated whether the final metal−iron oxide nanostructures had asymmetric core−shell or heterodimer morphologies, with the possibility to fine-tune the degree of exposure of the metal domain to the external environment. These in turn dictated the final shape of the NPs, that is, whether concave or nanocontainer-like structure.

We will discuss first iron oxide-only NPs obtained by leaching of Au. In the nanocontainers, structural and compositional analysis via transmission electron microscopy (TEM) indicated that the thin "membrane" surrounding part of the region was preserved as iron oxide after leaching of gold (Figure 1a−h) and had holes with diameters around 2−4 nm (Supporting Information Figure S4b). Such membrane was absent in the case of concave NPs (Figure 1d−f). Energy filtered elemental mapping analysis revealed the presence of iron and oxygen in the nanocontainers (Figure 1g,h). Furthermore, no gold was found in the elemental analysis of the NPs after gold removal, and both X-ray diffraction (XRD) patterns (which were compatible with both magnetite and maghemite structures) and UV−visible absorption spectra of the various samples were indistinguishable from those of spherical iron oxide NPs, thus overall excluding the presence of Au NPs (Figure 2a,b, see also Figure S4c,d of the Supporting Information).

From the magnetic hysteresis loops at room temperature (Figure 2c), both the Au−iron oxide parent NPs and those after Au leaching were superparamagnetic at room temperature, as deduced from the zero coercive field and the zero remanent magnetization. The ZFC-FC curves (Figure 2d) describe the temperature dependence of the magnetization. The ZFC curve provides information about the transition of the system between the blocked and the superparamagnetic state, which occurs at the temperature of the maximum magnetization, the blocking temperature (T_B). In the present case, no substantial difference was found in the samples before and after dissolution of gold, and for both systems a T_B value of 160 K was obtained. The curves for the two samples were indeed superimposable when using normalized units (Figure 2c,d).

When iron oxide was grown on top of AuPt alloy NPs, followed by annealing, AuPt−iron oxide heterostructures were formed, which exhibited clear epitaxial relationship between the iron oxide domain and the metal alloy domain (Figure 3 d). The Au and Pt metal proportions in AuPt after growing iron oxide were completely retained as those of the original AuPt alloy seeds (Supporting Information Figure S5). Leaching of Au from these NPs was also selective and complete. This time, because gold is relatively more reactive than platinum toward iodine,[39,40] the process left behind 1−3 nm sized Pt domains encased in the iron oxide cast (Figure 3a−c,e,f). In the nanocontainers, the Pt domains were located inside the cavity region, while in the case of concave NPs they were located inside the concave region (Figure 3e). XRD patterns of the AuPt/iron oxide heterodimers are shown in Figure 3 g. The UV−vis absorption spectra of all the NPs encasing Pt domains had features similar to those of the iron oxide NPs, due to the negligible contribution of the much smaller Pt domains to the overall absorption (Figure 3h).

3.2. "Destabilization" Experiments of Au Nanocrystals. In principle, each concave iron oxide NP can host one or more nano-objects having diameters smaller than or comparable to the concave region, and a question arises whether such temporary trapping can influence the fate of the nano-objects. In a series of experiments, a solution of concave iron oxide NPs was mixed with a solution of oleylamine-coated spherical Au nanocrystals that were respectively smaller (5 nm), bigger (20 nm), or matching in size the concave region of the iron oxide NPs (12 nm)

dx.doi.org/10.1021/ja108781w |J. Am. Chem. Soc. 2011, 133, 2205–2217

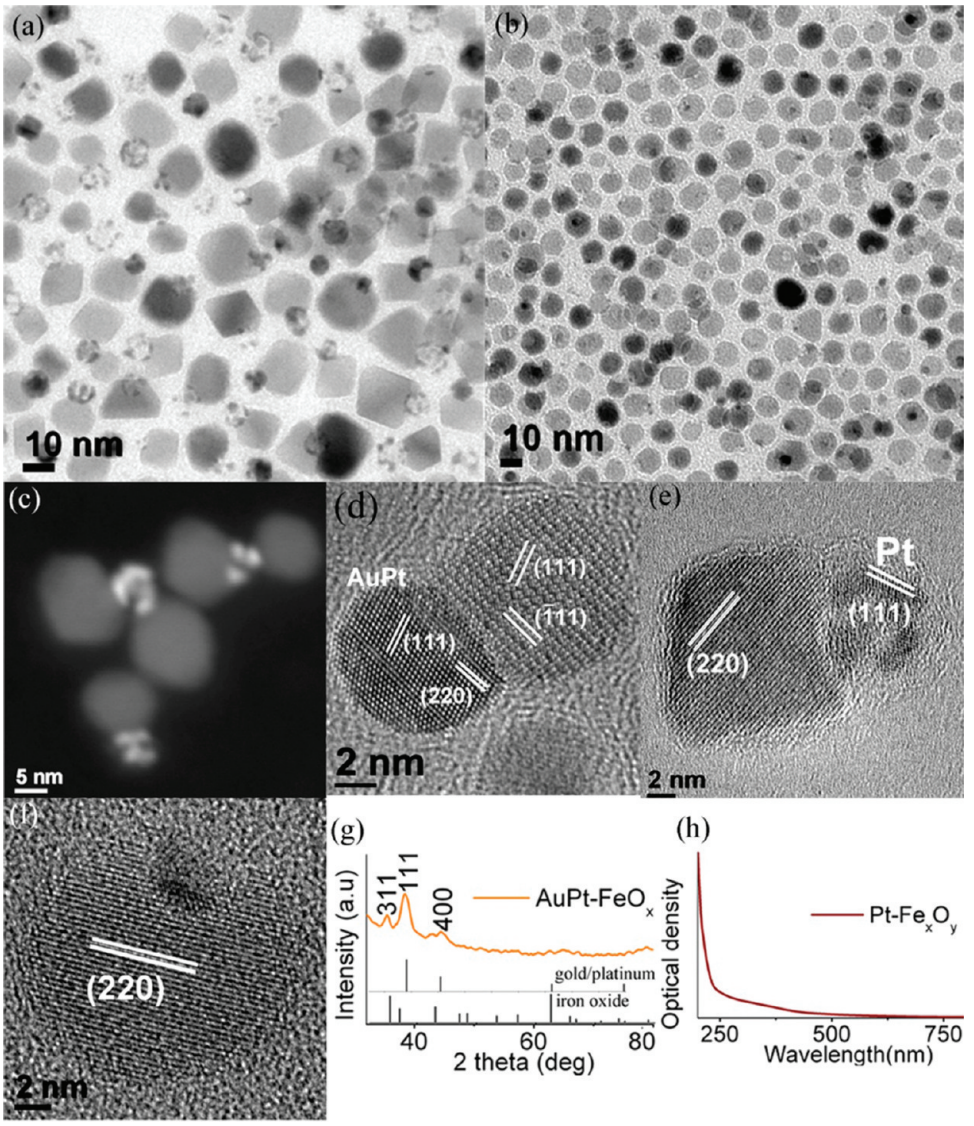

Figure 3. (a) TEM image of Pt−iron oxide nanocontainers; (b) TEM image of concave NPs encasing Pt domains, upon gold leaching; (c) HAADF-STEM image shows the encasement of Pt domains in nanocontainers after gold leaching; (d) HRTEM image of a starting AuPt−iron oxide heterodimer; (e) HRTEM image of an iron oxide nanocontainer encasing several Pt domains; (f) HRTEM image of a concave iron oxide NP encasing a single platinum domain; (g) XRD pattern of AuPt alloy/iron oxide heterodimers; and (h) UV−vis spectra of Pt−iron oxide nanocontainers after gold leaching from their parent heterodimers.

(Supporting Information Figure S6). These mixtures were then examined using TEM, absorption spectroscopy, and dynamic light scattering.

Our findings for the mixture of 5 nm Au nanocrystals and concave NPs are summarized in Figure 4. The TEM images of the mixture right after mixing (Figure 4a) and 3 h after (Figure 4b) did not show significant differences neither in size/shape of the Au nanocrystals nor of the concave NPs. In case of the 5 nm Au nanocrystals, the series of absorption spectra indicated clearly that the plasmon resonance of the gold did not shift over time (therefore no large Au nanocrystals were formed, see Figure 4c) and that all the spectra were basically a superposition of the absorption spectra of the pure solutions.

For the initial solutions of 5 nm Au nanocrystals, DLS measurements confirmed that the nanocrystals were present in solution as separate particles and not as aggregates (Figure 4d). For the solution of pure concave NPs, the situation was instead quite different, as they showed a strong tendency to clustering into aggregates of 500−1000 nm in size (Figure 4d). The reasons for such aggregation effect could be several. From one side, concave NPs might have a stronger tendency to interact with each other as a consequence of the leaching process, which could have stripped surfactant molecules also from areas on their surface that border the concave region. In addition to this, concave NPs might show in solution a tendency to stack close to each other similarly to the polymeric bowl-shaped microparticles reported recently by Dijkstra et al.[41] In the present case, for example, a portion of a concave NP could be weakly attracted by the concave region of a neighboring concave NPs. This observation was also in good agreement with the TEM images, in which the concave NPs were rarely seen as isolated particles, and instead the vast majority of them was present in the form of larger aggregates or stacks. Most likely, this aggregation is very dynamic in solution (i.e., NPs entangle and disentangle continuously).

dx.doi.org/10.1021/ja108781w |*J. Am. Chem. Soc.* 2011, 133, 2205–2217

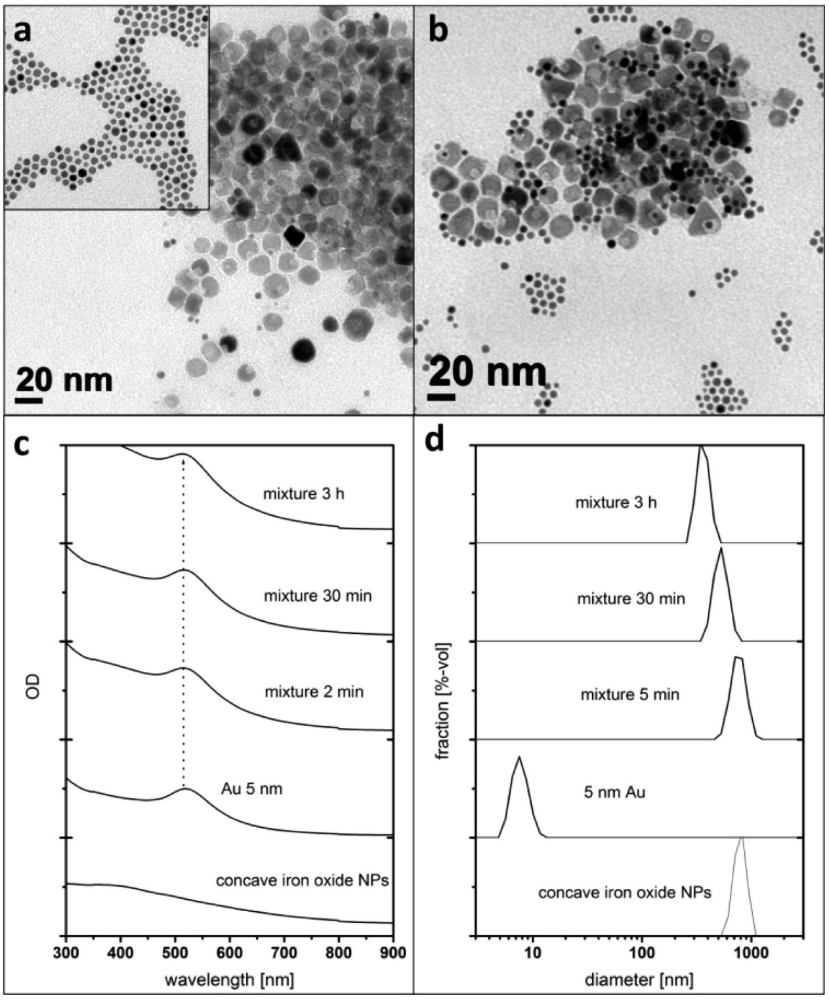

Figure 4. (a) TEM images of a mixture of 5 nm Au nanocrystals and concave NPs right after mixing (left, inset shows pure Au nanocrystals displayed at the same magnification as the main panel) and (b) 3 h after mixing. (c) Optical absorption spectra of the pure nanoparticle solutions (Au nanocrystals and concave NPs) and of their mixture at the times (after mixing) indicated in the figure. (d) DLS measurements of the pure nanoparticle solutions and of the mixture of the two after the times indicated in the figure. As a note, the aggregates of concave NPs (bottom DLS curve of panel d) could not be dissolved further, for example, via sonication.

The DLS measurements of the mixture of 5 nm Au nanocrystals and concave NPs are not straightforward to interpret, as at all times only aggregates of several hundreds of nanometers were detected, with a size similar to that of the original aggregates of concave NPs. In addition to that, especially for such small Au nanocrystals, it is not possible to detect via DLS free Au nanocrystals next to these aggregates (because the scattering intensity relates to r^6). Therefore, whether the Au nanocrystals were engulfed by the aggregates of concave NPs or they remained free in solution is unclear. Nevertheless, because both TEM and absorption measurements unequivocally showed that the gold nanocrystals were unchanged in size on a time scale of 3 h (and even for 24 h, see Supporting Information Figure S7), we conclude that their possible engulfment in the aggregates of concave NPs had no consequence on their size/stability.

For the mixture of concave NPs and Au nanocrystals matching in size with the concave region (12 nm), we found a substantially different behavior (Figure 5). TEM analysis of aliquots taken 1 min after mixing (Figure 5a) evidenced already a considerable increase in size polydispersity of the Au nanocrystals with respect to the original solution (Figure 5a, top right inset). Moreover, several dimer-shaped "key-lock" assemblies of Au nanocrystals trapped into concave NPs were present (see red circles in Figure 5a and its bottom left inset), which were not seen in the case of 5 nm Au nanocrystals discussed earlier. These assemblies are reminiscent of the recently reported key-lock assembly of polymeric NPs with shapes comparable to those of the NPs discussed here, and which involved depletion forces.[42] In the present case, the observed inclusion should also be due to favorable van der Waals interactions between the concave region of the NPs and the Au nanocrystals with a size matching the cavity.

The aliquot taken 3 h after mixing contained instead a significant fraction of extremely large Au nanocrystals (as seen by TEM) with sizes up to 100 nm, while the concave NPs had remained unchanged (Figure 5b). Absorption and DLS measurements confirmed that such size evolution of the Au nanocrystals was not a local effect observed only by TEM, nor it was a result of the specimen preparation, but it certainly took place in solution. Indeed, the various absorption spectra recorded at different times after mixing confirmed the size evolution of the Au nanocrystals (Figure 5c). While the absorption spectrum right after mixing was basically a superposition of the spectra of the pure solutions,

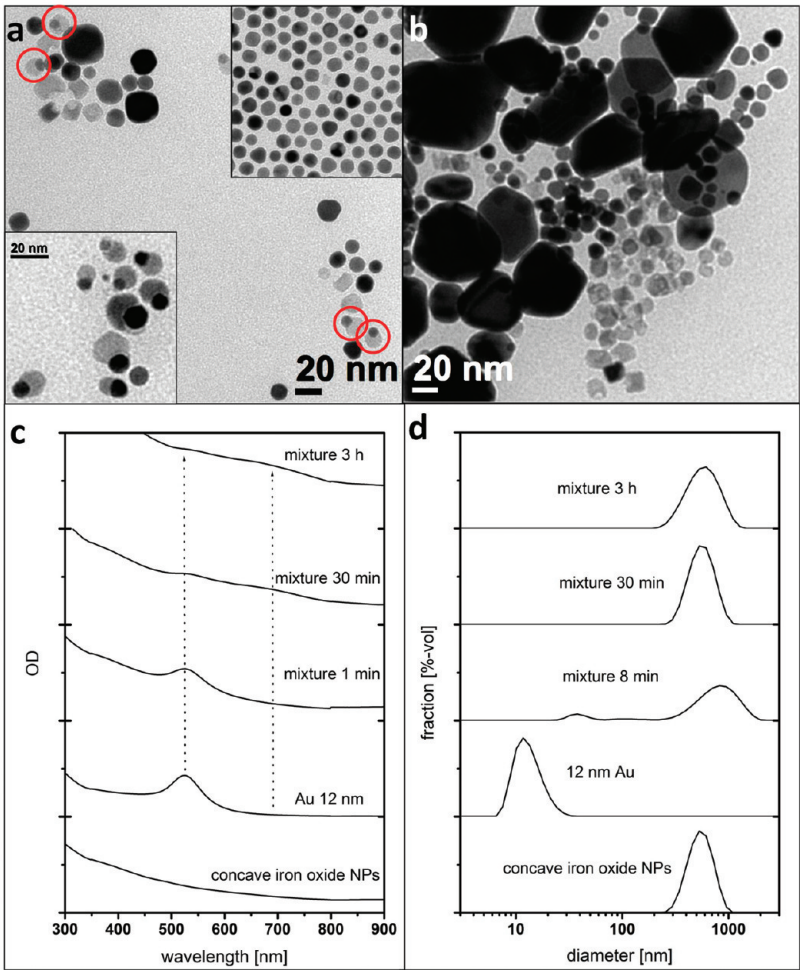

Figure 5. (a) TEM images of a mixture of 12 nm Au nanocrystals and concave NPs right after mixing (left, upper right inset shows pure Au nanocrystals displayed at the same magnification as the main panel, lower left inset shows magnified "key-lock" assemblies) and (b) 3 h after mixing (a TEM image that shows intermediate stages with agglomerated Au nanocrystals can be seen in Supporting Information Figure S8) . The red circles in (a) indicate key-lock assemblies, each made of one gold particle and one concave iron oxide NP. (c) Optical absorption spectra of the pure nanoparticle solutions and of the mixture of the two after the times indicated in the figure. (d) DLS measurements of the pure nanoparticle solutions and of the mixture of the two after the times indicated in the figure (see the Supporting Information for additional TEM images matching the times when absorption and DLS spectra were taken).

it changed remarkably 30 min later: the plasmon resonance at 525 had drastically lost intensity and a new absorption feature had appeared at around 700 nm, which could be correlated with the formation of very large Au nanocrystals as observed under TEM. DLS measurements of the pure Au solution (Figure 5d) confirmed that the size distribution of the initial sample was narrow and peaked at 12 nm; therefore, no fraction of large Au nanocrystals was present in it. Therefore, the large Au nanocrystals found at later stages after the mixing must had formed via a reaction induced by the concave NPs.

In this case too (12 nm Au nanocrystals), DLS measurements after mixing the two solutions were dominated by the big aggregates of concave NPs that were already present in the pure solution of concave NPs. Again, the scattering signal from 12 nm particles, even if one assumes that they were not engulfed in the aggregates, was by far lower in intensity and indeed undetectable with respect to that of such large aggregates. However, 8 min after the mixing, a scattering signal peaked at 40 nm was additionally seen, plus the original aggregates of concave NPs seemed to have widened in their size distribution (Figure 5d, third plot from the bottom). While it is clearly not possible to unambiguously assign all these features to specific species/events in solution, it is remarkable to note that these changes in DLS coincided in time with the evolution of an additional absorption band in the optical absorption spectra discussed above, and the occurrence of large Au particles in TEM images, which confirms that the Au size evolution was clearly taking place in solution. It is then likely that the scattering signal at around 40 nm was due to such growing Au nanocrystals. DLS measurements on the mixture at later stages (i.e., from 30 min on) looked again more like that of the original solution of concave NPs. In this case, the likely explanation is that the growing Au nanocrystals, which were transiently distinguishable in DLS, ended up forming large aggregates with the concave NPs. The interpretation of DLS data remains partially speculative, mainly due to the fact that the original concave iron oxide NPs already form big aggregates, which dominated the scattering behavior of the solution. Nevertheless, the combination with TEM and absorption measurements allowed us to conclude that the concave iron oxide NP were destabilizing the colloidal solution of 12 nm Au nanocrystals on a time scale of a couple of minutes, which finally resulted in a rather fast growth of the destabilized gold nanocrystals

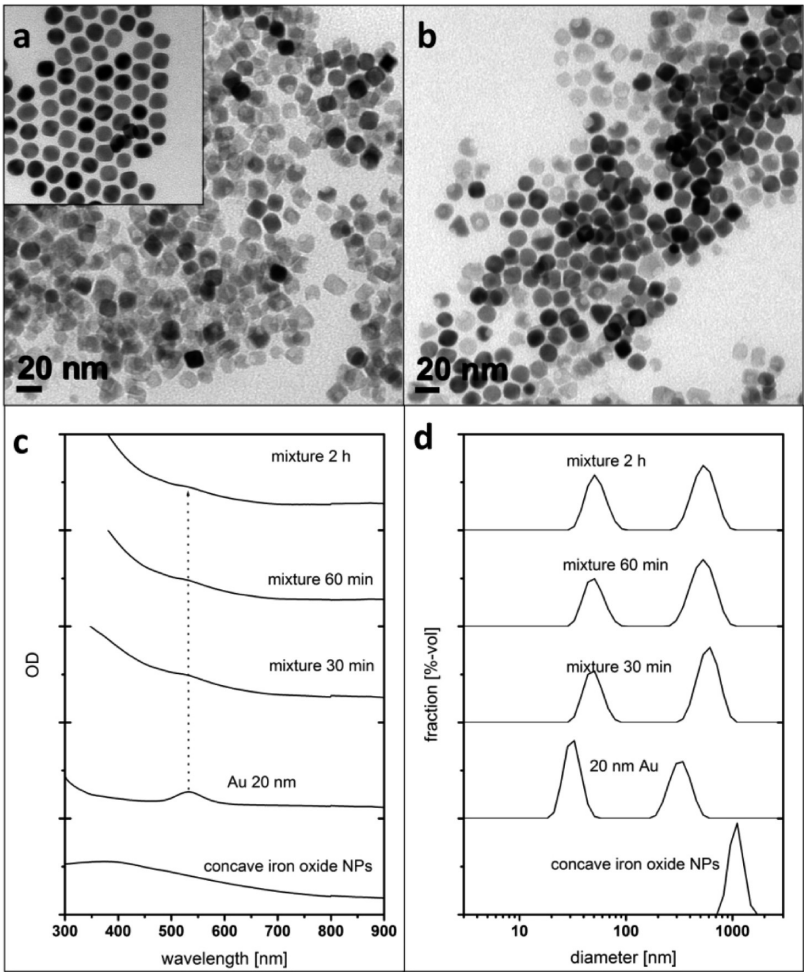

Figure 6. (a) TEM images of a mixture of 20 nm Au nanocrystals and concave NPs right after mixing (the inset shows pure Au nanocrystals at the same magnification) and (b) 3 h after mixing. (c) Optical absorption spectra of the pure nanoparticle solutions and of the mixture of the two after the times indicated in the figure.(d) DLS measurements of the pure nanoparticle solutions and of the mixture of the two after the times indicated in the figure.

(see Supporting Information Figure S8). Also, we would like to stress here that the engulfment of Au nanocrystals into the aggregates of concave NPs was supported by TEM analysis (see the Supporting Information) and highlighted the fact that those aggregates were highly dynamic in nature.

Finally, Figure 6 summarizes the results obtained by mixing the concave NPs with Au nanocrystals that were larger (20 nm diameter) than the concave region of the iron oxide NPs. Like in the case of 5 nm Au nanocrystals, TEM analysis of aliquots right after mixing and 3 h after mixing evidenced no significant differences with respect to the pristine sample; that is, the Au nanocrystals did not increase in size, and the concave NPs too remained unchanged (Figure 6a,b). Also, the plasmon resonance in the absorption spectra of the Au nanocrystals did not shift over time, proving that the Au nanocrystals had remained unchanged in the whole solution (Figure 6c). DLS indicated that pristine solutions of these large Au nanocrystals contained already some nanocrystal aggregates of 200−300 nm in size, in addition to the single 20 nm Au nanocrystals present as the major component (Figure 6d). However, by carefully evaluating TEM images, it could be concluded that these were aggregates of 20 nm Au nanocrystals (in clusters) and that no particles significantly larger than 20 nm were present.

The DLS measurements of the resulting solution after mixing were not straightforward to interpret: they indicated the presence of two different sizes of aggregates, one peaked at 40−50 nm and one at 500−600 nm. We tentatively assigned the first signal to small aggregates of the original 20 nm Au nanocrystals, as by TEM no larger Au nanocrystals were found, and the plasmon peak from the respective solution did not red-shift. The peak in DLS at 500−600 nm could be tentatively assigned to mixed aggregates of Au nanocrystals and concave NPs. Therefore, the combined data led to the conclusion that, similarly to the 5 nm Au nanocrystals, the 20 nm Au nanocrystals were basically unaffected in size by the presence of the concave NPs.

Overall, our findings from TEM, absorption spectra, and DLS measurements prove that the concave NPs displayed a strongly size selective reactivity toward Au nanocrystals: while larger and smaller Au nanocrystals remained completely intact over hours in the presence of the concave NPs, the ones that matched in size the concave region of the iron oxide NPs underwent a drastic size and morphological change within minutes.

3.3. Discussion on the Destabilization Mechanism. In addition to the experiments mentioned in the paragraph above, we conducted many control experiments, which allowed us to safely exclude that such a destabilization behavior for 12 nm Au

nanocrystals was seen in solutions of either "normal" iron oxide particles, or the parent heterodimer particles or nanocontainer particles. Furthermore, we carefully excluded that any residual iodine from the leaching process might be causing the observed effect (see the Supporting Information Figure S10). Hence, the whole set of experimental data suggests a mechanism of destabilization of Au nanocrystals that is operative only when concave iron oxide NPs are present and the size of the Au particles matches that of the concave region of these iron oxide NPs. Therefore, the mechanism of destabilization must be related to some type of interaction between the respective surfaces of the two types of NPs, and moreover such interaction seems to be suddenly maximized only when a nanocrystal fills entirely the concave region. Our assumption is that such interaction leads to mechanical friction between the concave NPs (the "lock") and the Au nanocrystals (the "key"), arising as a consequence of multiple trapping and detrapping events for each Au nanocrystal with the concave region, and that this friction can cause a partial loss of stabilizing molecules from its surface.

In support of this mechanism, there is first the evidence that the bigger (20 nm) Au nanocrystals were not affected by the concave NPs, which can be explained easily: a gold nanocrystal that is significantly bigger than the concave region of the NPs simply cannot enter this region. Therefore, the interaction of its surface with that of the concave NPs is extremely weak and not much different from that involving a "non-concave" particle (for example, a spherical nanocrystal).

For nanocrystals of a size that is well matching the concave region, the van der Waals interactions between the two particles are maximized, because for such arrangement all the distances between points on the concave surface of the iron oxide NP and points on the convex surface of the Au nanocrystal occupying the cavity are overall minimized. Moreover, also depletion attraction forces between the two particles are maximized in such arrangement, as these are entropic forces that scale according to the volume of excluded solvent. In this case, such volume is that of the entire cavity region, hence the highest possible volume of solvent that can be replaced by a particle.[42] This key-lock assembly corresponds therefore to a situation of minimal energy, with stabilizing molecules at the respective surfaces in close proximity being packed and well interlaced. It is therefore plausible that repetitive trapping and detrapping (the latter most likely due to thermal fluctuations) of Au nanocrystals from this concave region can cause friction between the respective surfaces (especially detrapping, because energy must be spent to displace the Au nanocrystal from a low energy configuration), which can lead to destabilization of the surface of the Au nanocrystals, as well as that of the concave region.

Such hypothesis becomes even more plausible if one looks at the key-lock dimers of Figure 5a: there is clearly no void space between the Au nanocrystals and the concave NPs, as one would expect from close-packed arrangements of surfactant-coated nanocrystals (surfactant molecules fill the space between nanocrystals, but are virtually transparent to the electron beam). This suggests that in each of these dimers the Au nanocrystal might have already lost a considerable number of ligands, at least those formerly present at the region on its surface that is now in close contact with the concave surface of its host.

In light of what has been said so far, it is also understandable why the Au nanocrystals that are much smaller than the concave region are not affected by the concave NPs. First, they can easily enter the concave region, swirl inside it, and exit the region, without any friction at all. Second, for Au nanocrystals with such a small radius of curvature, the internal surface of the concave region does not appear much different from the outer convex region of the same iron oxide NP. Therefore, in terms of van der Waals forces, the interaction of the Au nanocrystal with the concave surface is not much different from that with the outer convex surface of the same iron oxide NP, or even with that of a spherical (i.e., nonconcave) iron oxide NP. Also, when considering depletion forces, the entrapment of a small Au nanocrystal in a comparatively much larger concave region does not yield a significant decrease in free energy, as the volume of excluded solvent is minimal.

It is perhaps useful to identify as a macroscopic equivalent of our proposed mechanism that of "pencil sharpener". A sharpener obviously cannot sharpen pencils that are too narrow or too wide, but it works perfectly with pencils of the right size. In the case of NPs, the "sharpening" process by the concave particles results in a loss of surface ligands. It is true that "destabilized" nanocrystals can rebind to ligand molecules. However, due to the high dilution of these "freed" ligands in the solutions used in our experiments, it is actually more likely for the Au nanocrystals to aggregate with each other than to fully reacquire all the previously lost ligands and thus remain stable. In the literature, it is well documented that Au nanocrystals freed from their ligands can undergo various fusion/dissolution processes.[43] However, to our knowledge, the present reaction scheme involving concave NPs as destabilizing agents is the only one that can provide such an activation process with high size selectivity.

3.4. *cis*-Platin Loading Experiments. In this section, we report the results of experiments in which Au−iron oxide asymmetric core−shell nanocrystals and the corresponding nanocontainer NPs (i.e., after Au leaching) were tested as "containers" for the drug *cis*-platin. Experimental details have been discussed in section 2. After incubation of the nanocontainers with *cis*-platin, their surface was "wrapped" within an amphiphilic polymer shell, which guarantees the solubility of the nanocontainers in aqueous environment.[44,45] Additionally, the polymer coating might help to trap the *cis*-platin molecules loaded inside the cavity region of the nanocontainers. Using this approach and after carefully cleaning the NPs from excess *cis*-platin, we found an average of 1122 *cis*-platin molecules loaded per nanocontainer. When running control experiments using the parent core−shell gold−iron oxide NPs (i.e., before Au leaching to form the nanocontainers), only 173 molecules on average were loaded per NP. In this latter case, the loading should be due to a nonspecific adsorption of *cis*-platin on the surface of NPs; that is, the molecules were probably entrapped within the hydrophobic region of the polymer shell that coats the surface of the NPs. Therefore, the nanocontainers exhibited a loading capability that was 6.5 times higher than their parent NPs. These results suggest that, besides nonspecific adsorption, the higher loading capability of nanocontainers should be due to the presence of a cavity region, which appears to host a significant amount of *cis*-platin molecules. Also, no morphological variation of the nanocontainers was observed after *cis*-platin loading and water solubilization, as seen by TEM analysis (see Supporting Information Figure S13c,d), meaning that the thin iron oxide membrane of the cavity region was able to withstand the whole procedure.

It is worth comparing the *cis*-platin loading capacity of the present iron oxide nanocontainers with that of the porous NPs developed by Sun.[9] In the latter case, the loaded *cis*-platin amount was reported as Pt/Fe ratio (wt %), and the highest

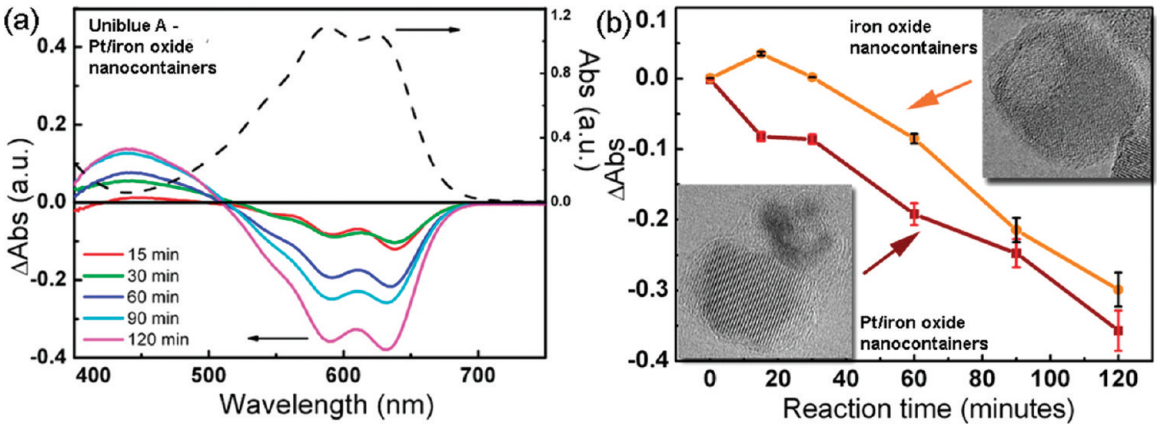

Figure 7. (a) Time-dependent evolution of difference absorption spectra (left axis) of a mixture of UBA and Pt/iron oxide nanocontainers ([UBA] = 10^{-5} M, total iron concentration = 3×10^{-3} M, as estimated by elemental analysis) in a N_2-saturated $CHCl_3$:EtOH (90:10 v/v) mixed solvent upon UV irradiation. Difference spectra were recorded by taking the freshly prepared unphotolized UBA-Pt/iron oxide nanocontainer solution as baseline. The absorption spectrum of a freshly prepared $CHCl_3$:EtOH UBA solution versus $CHCl_3$:EtOH is also shown (right axis). (b) Time course of UBA bleaching monitored at 588 nm. Data are reported as mean value of three replicates ± standard deviation. Inset: Representative TEM images of catalysts NPsx in the two samples.

value found was around 25%.[9] If expressed in the same way, the Pt/Fe ratio of the nanocontainers prepared by us was almost 10 times smaller (2.6%). Surely, the different geometries of the starting systems (a hollow porous sphere in Sun's work with respect to a nanocontainer made of a container region attached to a "non-hollow" iron oxide domain in our case) and the different coating procedures used in the two cases used account for the differences in the loading capability of the two systems. We noted, however, that the thin oxide membrane of our nanocontainers could be broken upon sonication for 10 min at low ultrasound power (100 W), yielding concave NPs (see Figure 1i and Supporting Information Figure S13a,b). This certainly represents an interesting aspect of the nanocontainers, with likely implications in drug delivery. Indeed, one requisite of all nanocarrier systems developed so far is that once the drug has been loaded into them and the carrier reaches the tumor, the drug has to be locally released to maximize the therapeutic efficiency and reduce the side effects. This has been achieved so far using stimuli-responsive drug delivery systems, which exploit physical stimuli like temperature or pH to promote the drug release.[46] In this context, mild sonication might represent an alternative external stimulus (sonication is indeed a medical practice already used on patients for destroying kidney stones).[47,48]

3.5. Photocatalytic Studies on Iron Oxide−Pt Nanocontainers. We tested the photoreduction of the UBA dye in the presence of nanocontainers (both iron oxide and Pt/iron oxide), as the dye undergoes a color change when changing from the oxidized anthraquinonic structure (blue) to the reduced hydroanthraquinonic structure (yellow), due to different electron conjugations in these two structures (see Figure S15 of the Supporting Information).[34] Figure 7a shows the time course of UBA photobleaching in the presence of the iron oxide−Pt nanocontainers in the deaerated $CHCl_3$:EtOH mixture, recorded as difference absorption spectra. The spectrum of UBA exhibited two characteristic peaks with λ'_{max} = 588 nm and λ''_{max} = 625 nm. A progressive bleaching in the 500−700 nm absorption region, corresponding to the disappearance of the ground state, and its concomitant conversion into the reduced form, could be observed over 120 min. Simultaneously, a new absorption signal appeared in the 400−500 nm region, which grew over time, and which was ascribable to the reduction of carbonyl groups of the anthraquinonic moiety of UBA.[49,50]

In Figure 7b, the evolution of the dye bleaching (taken at 588 nm, i.e., the most intense peak in the absolute spectrum) is reported for both iron oxide−Pt nanocontainers and iron oxide "only" nanocontainers, as a function of irradiation time. The data clearly evidence a stronger reducing capability of the iron oxide−Pt nanocontainers, in particular during the first 60 min of reaction. The enhancement of dye bleaching in the presence of Pt ranged from 40% to 60% as a function of reaction time. In both cases, the nanocontainers could be recovered from the cuvette by magnetic separation.

Various control experiments were carried out. First, no change occurred in solutions containing both UBA and nanocontainers if such solutions were simply stored in the dark. This clearly indicates that only photogenerated electrons could be responsible for the observed UBA bleaching. The photostability of both samples of nanocontainers, under the same experimental conditions used for bleaching experiments, was also tested. Both absorption spectra and TEM measurements of the irradiated samples confirmed that the main characteristics of the catalysts were retained (see Supporting Information Figures S14a,b and S15 for additional information).

A deaerated $CHCl_3$/EtOH mixture represents an ideal medium where reduction reactions can be effectively carried out, due to the efficient hole scavenging role of the solvent, which is able to suppress the production of $^{\bullet}OH$ radicals, and to the reducing action of conduction band electrons and $CH_3-CH^{\bullet}OH$ radicals. A direct involvement of $CH_3CH^{\bullet}OH$ and $^{\bullet}CCl_3$ species in the dye bleaching can be reasonably excluded,[51] as the initial dye absorption could be restored within 72 h upon reoxidation of UBA byproduct by ambient O_2. The observed UBA restoration, known to be driven by oxygen, suggests that the UBA bleaching proceeds through the reduction of carbonyl groups of the anthraquinonic moiety of UBA to yield the corresponding hydroanthraquinonic product, rather than the addition of $CH_3CH^{\bullet}OH$ groups (see also the Supporting Information).

Furthermore, the time evolution of UBA spectrum in the experiments did not show any significant shift of the typical absorption bands, which would have been a fingerprint of an oxidative reaction pathway.[51] Therefore, once the holes were rapidly scavenged by the solvent, excess electrons could be transferred in the Pt domains, thus improving the efficiency of electron−hole separation. In the presence of more efficient electron acceptors than the solvent molecules (i.e., UBA dye), the Pt domains could readily release the accumulated electrons, thus promoting the reduction process. Considering the narrow band gap of the iron oxide nanocontainers, recombination phenomena appear to be competitive with interfacial charge transfer.

4. CONCLUSIONS

We have reported the synthesis of concave-shaped and iron oxide nanocontainers and Pt−iron oxide NPs, starting from core/shell metal (either Au or AuPt)/iron oxide NPs, via a two-step process of annealing and Au leaching. We believe that the procedures reported here for the synthesis of concave NPs and nanocontainers can be extended to various metal oxide nanocrystalline materials. The concave NPs were found capable of destabilizing Au nanocrystals of sizes matching that of the concave region. This capability to act as destabilizers of NPs deserves certainly further scrutiny and eventually might be exploited for removal of NPs of specific sizes from contaminated fluids.

We also demonstrated that the iron oxide nanocontainers could be loaded with the antitumoral drug *cis*-platin. Ultrasound-triggered delivery of drugs is a subject of intensive research at present,[52,53] and the peculiarity of our systems to undergo rupture and cargo release upon sonication is under investigation in our laboratories in experiments involving tumor cells. The Pt/iron oxide nanostructures that we have reported could also serve as therapeutic agents, as in addition to the advantage of being manipulated by a magnetic field they already incorporate Pt NPs, which are potentially toxic toward cancer cells.

Finally, the nanocontainers encasing Pt domains were found to act as recoverable photocatalysts for the reduction of the model dye Uniblue A. Easy separability and reusability would greatly enhance the technological viability of NPs for real applications, contributing to solve the challenging issue of the catalyst recovery and to drive down the cost for materials,[54,55] and our nanocontainers represent a significant progress in this direction.

Overall, the important fields of applications targeted by us prove the potential of the nanostructures reported in this work.

■ ASSOCIATED CONTENT

Supporting Information. Additional details on structural characterization of the various nanostructures, on the various destabilization experiments, as well as on the photocatalytic and *cis*-platin loading experiments. This material is available free of charge via the Internet at http://pubs.acs.org.

■ AUTHOR INFORMATION

Corresponding Author
liberato.manna@iit.it

■ ACKNOWLEDGMENT

We acknowledge financial support from the European Union through the FP7 starting ERC grant NANO-ARCH (contract number 240111) and FP7 grant MAGNIFYCO (contract number NMP4-SL-2009-228622). We acknowledge Mauro Povia for assistance with the X-ray diffraction experiments and Nobutaka Maeda for helpful discussion.

■ REFERENCES

(1) Figuerola, A.; Di Corato, R.; Manna, L.; Pellegrino, T. *Pharmacol. Res.* **2010**, *62*, 126–143.
(2) Safran, S. A. *Nat. Mater.* **2003**, *2*, 71–72.
(3) Chen, J.; Xu, L. N.; Li, W. Y.; Gou, X. L. *Adv. Mater.* **2005**, *17*, 582–586.
(4) Zeng, S. Y.; Tang, K. B.; Li, T. W.; Liang, Z. H.; Wang, D.; Wang, Y. K.; Zhou, W. W. *J. Phys. Chem. C* **2007**, *111*, 10217–10225.
(5) Zhang, L.; Gu, F. X.; Chan, J. M.; Wang, A. Z.; Langer, R. S.; Farokhzad, O. C. *Clin. Pharm. Ther.* **2008**, *83*, 761–769.
(6) Herzing, A. A.; Kiely, C. J.; Carley, A. F.; Landon, P.; Hutchings, G. J. *Science* **2008**, *321*, 1331–1335.
(7) Weinstein, J. S.; Varallyay, C. G.; Dosa, E.; Gahramanov, S.; Hamilton, B.; Rooney, W. D.; Muldoon, L. L.; Neuwelt, E. A. *J. Cereb. Blood Flow Metab.* **2010**, *30*, 15–35.
(8) Lee, J. H.; et al. *Nat. Med.* **2007**, *13*, 95–99.
(9) Cheng, K.; Peng, S.; Xu, C. J.; Sun, S. H. *J. Am. Chem. Soc.* **2009**, *131*, 10637–10644.
(10) Shin, J. M.; Anisur, R. M.; Ko, M. K.; Im, G. H.; Lee, J. H.; Lee, I. S. *Angew. Chem., Int. Ed.* **2009**, *48*, 321–324.
(11) MacDonald, J. E.; Sadan, M. B.; Houben, L.; Popov, I.; Banin, U. *Nat. Mater.* **2010**, *9*, 810–815.
(12) An, K.; Hyeon, T. *Nano Today* **2009**, *4*, 359–373.
(13) Kim, K. T.; Meeuwissen, S. A.; Nolte, R. J. M.; van Hest, J. C. M. *Nanoscale* **2010**, *2*, 844–858.
(14) Cabot, A.; Puntes, V. F.; Shevchenko, E.; Yin, Y.; Balcells, L.; Marcus, M. A.; Hughes, S. M.; Alivisatos, A. P. *J. Am. Chem. Soc.* **2007**, *129*, 10358–10360.
(15) Lee, Y. M.; Garcia, M. A.; Huls, N. A. F.; Sun, S. H. *Angew. Chem., Int. Ed.* **2010**, *49*, 1271–1274.
(16) Wang, D.; Lippard, S. J. *Nat. Rev. Drug Discovery* **2005**, *4*, 307–320.
(17) Galanski, M.; Arion, V. B.; Jakupec, M. A.; Keppler, B. K. *Curr. Pharm. Des.* **2003**, *9*, 2078–2089.
(18) Dhar, S.; Gu, F. X.; Langer, R.; Farokhzad, O. C.; Lippard, S. J. *Proc. Natl. Acad. Sci. U.S.A.* **2008**, *105*, 17356–17361.
(19) Matsumura, S.; Ajima, K.; Yudasaka, M.; Iijima, S.; Shiba, K. *Mol. Pharmaceutics* **2007**, *4*, 723–729.
(20) Hirai, M.; et al. *Int. J. Pharm.* **2010**, *391*, 274–283.
(21) Aryal, S.; Hu, C.-M. J.; Zhang, L. *ACS Nano* **2009**, *4*, 251–258.
(22) Oishi, M.; Hayashi, H.; Michihiro, I. D.; Nagasaki, Y. *J. Mater. Chem.* **2007**, *17*, 3720–3725.
(23) Guo, R.; Zhang, L.; Qian, H.; Li, R.; Jiang, X.; Liu, B. *Langmuir* **2010**, *26*, 5428–5434.
(24) Taylor, A.; Krupskaya, Y.; Krämer, K.; Füssel, S.; Klingeler, R.; Büchner, B.; Wirth, M. P. *Carbon* **2010**, *48*, 2327–2334.
(25) Arruebo, M.; Fernández-Pacheco, R.; Ibarra, M. R.; Santamaría, J. *Nano Today* **2007**, *2*, 22.
(26) Bedja, I.; Kamat, P. V. *J. Phys. Chem.* **1995**, *99*, 9182–9188.
(27) Awazu, K.; Fujimaki, M.; Rockstuhl, C.; Tominaga, J.; Murakami, H.; Ohki, Y.; Yoshida, N.; Watanabe, T. *J. Am. Chem. Soc.* **2008**, *130*, 1676–1680.
(28) Yu, T.; Zeng, J.; Lim, B.; Xia, Y. N. *Adv. Mater.* **2010**, *22*, 5188–5192.
(29) Cozzoli, P. D.; Comparelli, R.; Fanizza, E.; Curri, M. L.; Agostiano, A.; Laub, D. *J. Am. Chem. Soc.* **2004**, *126*, 3868–3879.
(30) Ismail, A. A.; Bahnemann, D. W.; Bannat, I.; Wark, M. *J. Phys. Chem. C* **2009**, *113*, 7429–7435.
(31) Lin, D. D.; Wu, H.; Zhang, R.; Pan, W. *Chem. Mater.* **2009**, *21*, 3479–3484.
(32) Elmaletn, E.; Saunders, A. E.; Costi, R.; Salant, A.; Banin, U. *Adv. Mater.* **2008**, *20*, 4312–4317.

(33) Amirav, L.; Alivisatos, A. P. *J. Phys. Chem. Lett.* **2010**, *1*, 1051–1054.
(34) Cozzoli, P. D.; Comparelli, R.; Fanizza, E.; Curri, M. L.; Agostiano, A. *Mater. Sci. Eng., C* **2003**, *23*, 707–713.
(35) Yu, H.; Chen, M.; Rice, P. M.; Wang, S. X.; White, R. L.; Sun, S. H. *Nano Lett.* **2005**, *5*, 379–382.
(36) Wei, Y. H.; Klajn, R.; Pinchuk, A. O.; Grzybowski, B. A. *Small* **2008**, *4*, 1635–1639.
(37) Lu, X. M.; Tnan, H. Y.; Korgel, B. A.; Xia, Y. N. *Chem.-Eur. J.* **2008**, *14*, 1584–1591.
(38) Deka, S. R.; Quarta, A.; Di Corato, R.; Falqui, A.; Manna, L.; Cingolani, R.; Pellegrino, T. *Langmuir* **2010**, *26*, 10315–10324.
(39) Kelsall, G. H.; Welham, N. J.; Diaz, M. A. *J. Electroanal. Chem.* **1993**, *361*, 13–24.
(40) Berry, G. M.; Bothwell, M. E.; Bravo, B. G.; Cali, G. J.; Harris, J. E.; Mebrahtu, T.; Michelhaugh, S. L.; Rodriguez, J. F.; Soriaga, M. P. *Langmuir* **1989**, *5*, 707–713.
(41) Marechal, M.; Kortschot, R. J.; Demirors, A. F.; Imhof, A.; Dijkstra, M. *Nano Lett.* **2010**, *10*, 1907–1911.
(42) Sacanna, S.; Irvine, W. T. M.; Chaikin, P. M.; Pine, D. J. *Nature* **2010**, *464*, 575–578.
(43) Zhou, J. F.; Sedev, R.; Beattie, D.; Ralston, J. *Langmuir* **2008**, *24*, 4506–4511.
(44) Pellegrino, T.; et al. *Nano Lett.* **2004**, *4*, 703–707.
(45) Di Corato, R.; Quarta, A.; Piacenza, P.; Ragusa, A.; Figuerola, A.; Buonsanti, R.; Cingolani, R.; Manna, L.; Pellegrino, T. *J. Mater. Chem.* **2008**, *18*, 1991–1996.
(46) Ganta, S.; Devalapally, H.; Shahiwala, A.; Amiji, M. *J. Controlled Release* **2008**, *126*, 187–204.
(47) Bailey, M. R.; Khokhlova, V. A.; Sapozhnikov, O. A.; Kargl, S. G.; Crum, L. A. *Acoust. Phys.* **2003**, *49*, 369–388.
(48) Patlas, M.; Farkas, A.; Fisher, D.; Zaghal, I.; Hadas-Halpern, I. *Br. J. Radiol.* **2001**, *74*, 901–904.
(49) Dryhurst, G.; Kadish, K. M.; Scheller, F.; Renneberg, R. *Biological Electrochemistry*; Academic Press Inc.: New York, 1982; Vol. 1, pp 1−115.
(50) Washburn, E. W. *International Critical Tables of Numerical Data, Physics, Chemistry and Technology*; McGraw Hill: New York, 1926−1930.
(51) Cozzoli, P. D.; Fanizza, E.; Comparelli, R.; Curri, M. L.; Agostiano, A.; Laub, D. *J. Phys. Chem. B* **2004**, *108*, 9623–9630.
(52) Epstein-Barash, H.; Orbey, G.; Polat, B. E.; Ewoldt, R. H.; Feshitan, J.; Langer, R.; Borden, M. A.; Kohane, D. S. *Biomaterials* **2010**, *31*, 5208–5217.
(53) Lentacker, I.; Geers, B.; Demeester, J.; De Smedt, S. C.; Sanders, N. N. *Mol. Ther.* **2010**, *18*, 101–108.
(54) Ye, M. M.; Zhang, Q. A.; Hu, Y. X.; Ge, J. P.; Lu, Z. D.; He, L.; Chen, Z. L.; Yin, Y. D. *Chem.-Eur. J.* **2010**, *16*, 6243–6250.
(55) Beydoun, D.; Amal, R.; Scott, J.; Low, G.; McEvoy, S. *Chem. Eng. Technol.* **2001**, *24*, 745–748.